

# IN2LAAMA: INertial Lidar Localisation Autocalibration And Mapping

Cedric Le Gentil, *Member, IEEE*, Teresa Vidal-Calleja, *Member, IEEE*, and Shoudong Huang, *Senior Member, IEEE*

**Abstract**—In this paper, we present INertial Lidar Localisation Autocalibration And Mapping (IN2LAAMA): a probabilistic framework for localisation, mapping, and extrinsic calibration based on a 3D-lidar and a 6-DoF-IMU. Most of today's lidars collect geometric information about the surrounding environment by sweeping lasers across their field of view. Consequently, 3D-points in one lidar scan are acquired at different timestamps. If the sensor trajectory is not accurately known, the scans are affected by the phenomenon known as motion distortion. The proposed method leverages preintegration with a continuous representation of the inertial measurements to characterise the system's motion at any point in time. It enables precise correction of the motion distortion without relying on any explicit motion model. The system's pose, velocity, biases, and time-shift are estimated via a full batch optimisation that includes automatically generated loop-closure constraints. The autocalibration and the registration of lidar data relies on planar and edge features matched across pairs of scans. The performance of the framework is validated through simulated and real-data experiments.

**Index Terms**—Lidar, inertial measurement unit, IMU, localisation, mapping, SLAM, calibration

## I. INTRODUCTION

LOCALISATION and mapping is a key component of any autonomous system operating in unknown or partially known environments. In a world that relies more and more on automation and robotics, the need for 3D models of the environment is increasing at a fast pace. Autonomous systems navigation is not the only source of demand for 3D maps. A growing number of fields are gaining interest in dense and accurate representations especially for monitoring or inspection operations, and augmented reality purposes. This manuscript presents a probabilistic framework for localisation and mapping with targetless extrinsic calibration that tightly integrates data from a 3D-lidar range scanner and a 6-DoF-Inertial Measurement Unit (IMU). We have named this approach *INertial Lidar Localisation Autocalibration And Mapping* (IN2LAAMA). Fig. 1 shows an example of the system and multiple views of a map generated with the proposed method.

In its early days, as shown in [1], localisation of autonomous vehicles was mainly relying on the knowledge of the position of beacons in the environment. The same concept is used by GPS, where multiple satellites orbiting more than twenty

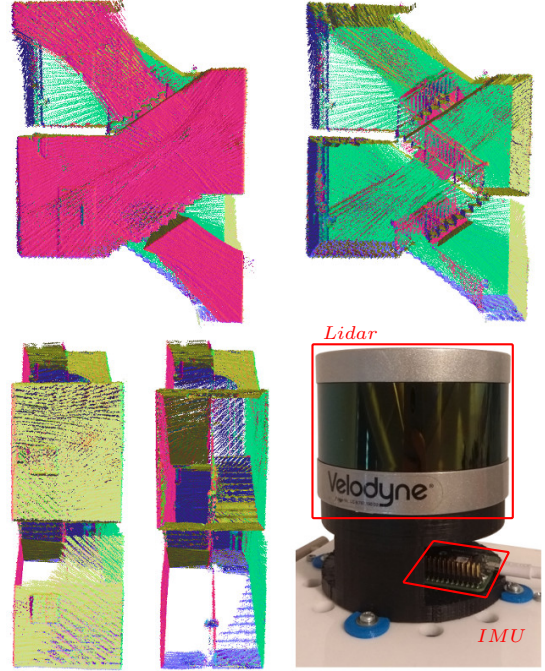


Fig. 1: Example of map generated with IN2LAAMA in a staircase. Bottom right is the sensor suite used (Velodyne VLP-16 lidar and Xsens MTi-3 IMU).

thousands kilometres above our heads serve as beacons. While GPS provides substantial localisation information in many outdoor environments worldwide, it cannot be used indoors or in scenarios where line-of-sight with the satellites cannot be guaranteed. The non-stopping evolution of lidar technologies in the past decades permitted great advancements in the simultaneous localisation and mapping field. Despite providing crucial information about real-world geometry, nowadays 3D-lidars still suffer from some drawbacks. Due to its sweeping mechanism (be it with the help of a spinning mechanism, actioned mirrors, prisms, etc) a lidar does not take a snapshot of the environment but progressively scans the surrounding space. Accurate knowledge of the motion of the sensor during the sweeps is needed to allow the grouping of the collected 3D-points in consistent scans. Inaccuracies in the trajectory will introduce *motion distortion* in the resulting point cloud.

By leveraging inertial data, the proposed method aims to accurately correct motion distortion in lidar scans without making explicit assumptions about the system's motion. In

The authors are with the Centre for Autonomous Systems at the Faculty of Engineering and IT, University of Technology Sydney, Australia. Email: cedric.legentil@student.uts.edu.au, {teresa.vidalcalleja, shoudong.huang}@uts.edu.au

Manuscript received Month DD, YYYY; revised Month DD, YYYY.

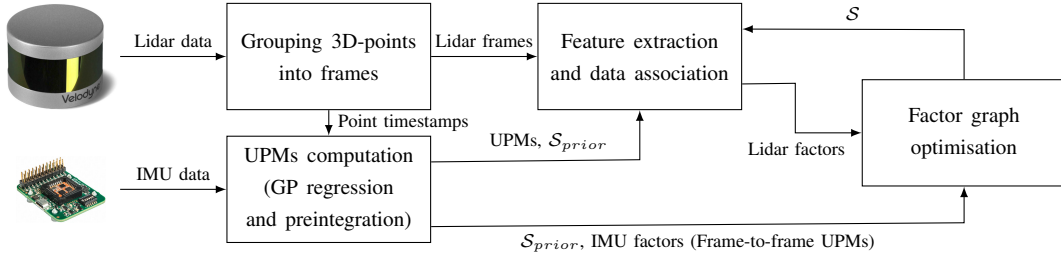


Fig. 2: Overview of IN2LAAMA with  $S$  the estimated state.

this work, as introduced in [2], the concept of preintegration ([3], [4]) is used over interpolated IMU measurements. These generated pseudo-measurements are named Upsampled Preintegrated Measurements (UPMs) and allow the generation of inertial data at any time. Gaussian Process (GP) inference is used for non-parametric probabilistic interpolation. UPMs inherit all the properties from the original preintegration [3], which include the independence of the measurements with respect to the initial pose and velocity conditions.

As for most localisation and mapping frameworks, a front-end for feature extraction and data association, and a back-end for state estimation through numerical optimisation are the two main modules of the proposed framework. Nonetheless, IN2LAAMA differs from most frameworks as per the tight relationship between these two major modules. Reliable geometric feature extraction in lidar scans requires the knowledge of the system's trajectory to be unaffected by motion distortion. Accurate knowledge of the system's trajectory relies on the extraction and association of robust features. To address this “chicken-and-egg” problem, the features (front-end) are periodically recomputed according to the last state estimate (back-end), as shown in the block diagram of Fig. 2.

Our work does not aim at real-time operation but focuses on accurate 3D mapping given no prior knowledge. Therefore, an offline batch optimisation framework is proposed here. This paper extends our previous work on lidar-inertial localisation and mapping [5]. The key contribution with respect to our previous work is the use of IMU factors between consecutive poses and velocities of the estimated state. These additional constraints in the optimisation generalise the full formulation of lidar-inertial integration for localisation and mapping and provide more accurate results. This paper also contains an extensive analysis of the impact of lidar-inertial fusion in the presence of inaccurate extrinsic calibration and poorly modelled inertial data. The second important contribution of this work is the ability to perform targetless extrinsic calibration between a 3D-lidar and a 6-DoF IMU simultaneously to localisation and mapping. A simple loop-closure detection method along with better outlier rejection strategies have been integrated in the proposed framework.

The remainder of the paper is organised as follows. Section II discusses related work. The method overview is given in Section III. The back-end of IN2LAAMA is explained in Section IV. Section V details the front-end of the method. In Section VI, we explain implementation details and the strategy employed for building our optimisation problem. Section VII

presents simulated and real-world experimental results. This paper comes along a video that shows 3D animations of the results in real-world scenarios. Finally, conclusion and future work are discussed in Section VIII.

## II. RELATED WORK

Lidar scan geometric registration is the foundation of most of the laser-based localisation algorithms out there. The introduction of Iterative Closest Points (ICP) [6] and generalised ICP [7] allowed the estimation of the rigid transformation between two point clouds. The method presented in [8] estimates a system trajectory using ICP for frame-to-frame relative poses estimation, and a pose-graph formulation to correct the drift inherent to odometry-like frameworks. This method, among others, does not address the phenomenon of motion distortion in lidar scans.

Different approaches have been presented in the literature for state estimation of moving lidar/rolling-shutter sensors. In [9], the authors extended the 2D standard ICP to account for the lidar motion during the sweep, based on the assumption of constant velocity. This assumption about the system motion is often used in the literature as in [10] and [11]. Both techniques rely on linear pose-interpolation between control points. In many real-world scenarios, these motion model assumptions do not represent the true nature of the system's motion.

In [12], the authors use a linear combination of temporal basis functions to represent the state. While providing greater representability compared to traditional discrete models, the performances of continuous state estimation frameworks depend on the veracity of the models assumed. Nonetheless, continuous pose representation, as introduced in [11] or [12], allows the use of non-synchronised sensors in multi-modal frameworks.

A probabilistic approach for continuous state estimation is presented in [13]. In this method, the use of computationally efficient GP regression over a discrete maximum a posteriori estimation allows the state variables to be queried at any point in time. While allowing continuous inference, this method still relies on discrete state estimation.

To reach real-time operations, techniques like [10] and [14] consider the correction of motion distortion at the front-end level and not as part of the estimation problem. In other words, the prior knowledge of the actual motion is used to undistort the incoming point clouds, but no other action is conducted later to improve the distortion correction according to the new state estimate. With such a strategy, there is a risk of

accumulating drift due to inaccurate initial conditions. Our proposed framework constantly revisits the motion distortion correction all along the estimation process.

While unreliable for long-run motion estimation on their own, IMUs have been extensively used in combination with exteroceptive sensors like cameras and lidars to develop robust multi-modal systems. Initially proposed for visual-inertial fusion in [3] and [4], the concept of preintegration allows the pre-processing of inertial measurements for state estimation. The key idea is to dissociate the acceleration integration from the initial pose and velocity. By doing so, the inertial integrations can be computed beforehand and the resulting pseudo-measurements stay constant during the estimation process, regardless of the linearisation point changes. In our earlier work on lidar-IMU extrinsic calibration [2], we extended this concept by considering preintegration over continuous representation of the inertial data. The UPMs allow the computation of inertial data at any timestamp and therefore, enable the characterisation of the system's motion during a lidar scan without the use of any explicit motion/state-model. The localisation and mapping work presented here leverages the UPMs in a graph-based optimisation framework that does not rely on any explicit motion model.

The 3D-maps generated in [15] and [16] make use of surfels. Given dense enough 3D-point clouds, surfels can provide rich surface information. Various front-end solutions have been explored in the literature to deal with the sparsity of 3D-data generated by nowadays lidars. The approach presented in [17] estimates both the system trajectory and the position of planes in the environment based on a novel plane representation. Such formulation reduces the complexity of the optimisation problem and filters the individual measurements' noise. But this method is adapted solely to highly structured environments. The authors of [18] proposed a lidar feature extraction method that efficiently detects planes and 3D-lines in structured environments. Using a specific sampling of lidar scans, IMLS-SLAM [19] leverage more generic "features", and can be used in weakly structured environments. The channel-by-channel feature extraction introduced in LOAM [10] does not require the computation of surface information (normals) for each of the lidar points. Consequently, this approach is suitable for lidars with lower resolution and inspired our front-end development.

Most of the localisation and mapping techniques mentioned above rely on known extrinsic calibration between the different sensors of the system. Despite the popularity of lidars and IMUs, the calibration between these sensors has not been extensively studied. Our previous work [2] proposed a calibration process based on a simple calibration target (a set of planes). As a general rule, the use of calibration targets allows the calibration frameworks to leverage prior knowledge of the data observed during the calibration recording. For example, the visual-inertial calibration method presented in [20] uses a known checkerboard to determine the camera position. Few problems can arise from the fact of using a calibration target. The first one is the manufacture of the target itself. An imprecise target leads to inaccurate calibration parameters. The second, and maybe the most important issue

in an industrial/commercial context, is the need for a dedicated calibration procedure with a specific calibration rig. In other words, it means that a user, or often a qualified operator, needs to perform a series of pre-defined actions to re-calibrate the system. Work has been conducted to move toward targetless calibration procedures in the case of lidar-visual calibration ([21] [22]). Our proposed method follows this line of thought by allowing targetless extrinsic calibration of a 3D-lidar and a 6-DoF-IMU, thus removing the need for a dedicated calibration rig/environment/pre-defined actions.

### III. METHOD OVERVIEW

#### A. Notation and definitions

Let us consider a rigidly mounted 3D lidar and a 6-DoF IMU. The lidar and IMU reference frames at time  $t_i$  are respectively noted  $\mathfrak{F}_L^{t_i}$  and  $\mathfrak{F}_I^{t_i}$ . The relative transformation between the two sensors is characterised by the rotation matrix  $\mathbf{R}_I^L$  and the translation vector  $\mathbf{p}_I^L$ . Homogeneous transformation will be used for the rest of the paper, therefore rotation matrices and translations/positions will be associated with  $4 \times 4$  transformation matrices with the same combination of subscripts and superscripts,

$$\mathbf{T}_a^b = \begin{bmatrix} \mathbf{R}_a^b & \mathbf{p}_a^b \\ \mathbf{0}^\top & 1 \end{bmatrix} \text{ and } \mathbf{T}_a^{b^{-1}} = \begin{bmatrix} \mathbf{R}_a^b{}^\top & -\mathbf{R}_a^b{}^\top \mathbf{p}_a^b \\ \mathbf{0}^\top & 1 \end{bmatrix}. \quad (1)$$

The 3D-points  $\mathbf{x}_L^i$  provided by the lidar at time  $t_i$  are projected from  $\mathfrak{F}_L^{t_i}$  to  $\mathfrak{F}_I^{t_i}$  using

$$\begin{bmatrix} \mathbf{x}_I^i \\ 1 \end{bmatrix} = \mathbf{T}_I^L \begin{bmatrix} \mathbf{x}_L^i \\ 1 \end{bmatrix}. \quad (2)$$

In this work, the lidar points are grouped into  $M$  frames. Note that in the proposed method, a frame corresponds to the data collected in scan greater than 360-degree as explained in Section V-C. The points belonging to the  $m^{\text{th}}$  frame form the set  $\mathcal{X}^m$ .  $\mathcal{F}^m$  is a subset of  $\mathcal{X}^m$  that represents lidar feature-points. A feature is a point belonging to a distinctive type of surface (e.g. plane or edge). The set of feature associations  $\mathcal{A}$  contains tuples of 3 or 4 lidar feature-points depending on whether they are edges or planes respectively.

The 6-DoF-IMU is the combination of a 3-axis accelerometer and a 3-axis gyroscope. Therefore, the inertial data acquired consists of proper accelerations  $\mathbf{f}_i$  and angular velocities  $\boldsymbol{\omega}_i$  at time  $t_i$  ( $i = 1, \dots, Q$ ). GP regression is used to infer inertial readings on each IMU DoF independently at any given time  $t$ . The continuous  $\mathbf{f}^*(t)$  and  $\boldsymbol{\omega}^*(t)$  readings estimated using GPs allow the attribution of IMU readings to each of the individual lidar points.

The proposed method aims to estimate the IMU orientation  $\mathbf{R}_W^{\tau_m}$ , position  $\mathbf{p}_W^{\tau_m}$  and velocity  $\mathbf{v}_W^{\tau_m}$  for each lidar frame  $m = (0, \dots, M-1)$ , as well as the IMU biases and the time-shifts between the two sensors. The subscript  $W$  represents the earth-fixed world reference frame  $\mathfrak{F}_W$ , and  $\tau_m$  corresponds to the timestamp at the beginning of the  $m^{\text{th}}$  lidar frame.  $\mathfrak{F}_\bullet^{\tau_m}$  refers to the reference frame of the IMU or lidar (as  $\bullet$  represents in this case  $L$  or  $I$ ) at time  $\tau_m$ .

In the following,  $\mathcal{S}$  indicates the state to be estimated:  $\mathcal{S} = (\mathbf{R}_W^{\tau_0}, \dots, \mathbf{R}_W^{\tau_{M-1}}, \mathbf{p}_W^{\tau_0}, \dots, \mathbf{p}_W^{\tau_{M-1}}, \mathbf{v}_W^{\tau_0}, \dots, \mathbf{v}_W^{\tau_{M-1}},$

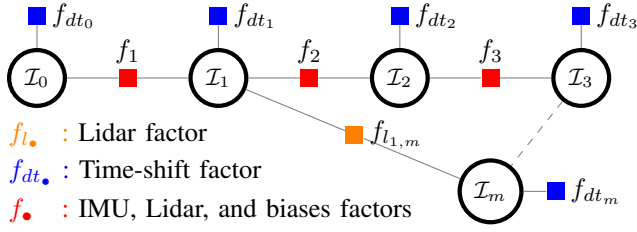


Fig. 3: Factor graph representation of the optimisation problem solved in IN2LAAMA.  $\mathcal{I}_m = \{\mathbf{R}_W^{\tau_m}, \mathbf{p}_W^{\tau_m}, \mathbf{v}_W^{\tau_m}, \hat{\mathbf{b}}_f^m, \hat{\mathbf{b}}_\omega^m, \hat{\delta}_t^m\}$  represents the IMU pose, velocity, biases and time-shift correction associated to the lidar scan  $\mathcal{X}^m$  at  $\tau_m$ . The factor  $f_{l2,m}$  represents a loop-closure.

$\hat{\mathbf{b}}_f^0, \dots, \hat{\mathbf{b}}_f^{M-1}, \hat{\mathbf{b}}_\omega^0, \dots, \hat{\mathbf{b}}_\omega^{M-1}, \hat{\delta}_t^0, \dots, \hat{\delta}_t^{M-1}$  with  $\hat{\mathbf{b}}_f^m, \hat{\mathbf{b}}_\omega^m$ , and  $\hat{\delta}_t^m$  the biases and time-shift corrections associated to the  $m^{\text{th}}$  lidar frame (more details are given in Section IV-C). In the case of extrinsic autocalibration, the calibration parameters  $\mathbf{T}_f^L$  are also added to  $\mathcal{S}$ . The calibration procedure is explained in Section VI-B.

### B. Cost function

The localisation and mapping problem is formulated as a Maximum Likelihood Estimation (MLE):

$$\mathcal{S}^* = \underset{\mathcal{S}}{\operatorname{argmin}} -\log(p(\mathcal{S}|\mathcal{Z})) = \underset{\mathcal{S}}{\operatorname{argmin}} C(\mathcal{S}), \quad (3)$$

with  $\mathcal{Z}$  representing the available measurements and  $C$  the optimisation cost function.

Represented as the factor graph in Fig. 3, and under the assumption of zero-mean Gaussian noise, the estimation can be solved by minimising geometric distances  $d_a$  associated with lidar features, inertial residuals  $\mathbf{r}_f^m$ , accelerometer biases residuals  $\mathbf{r}_f^m$ , gyroscope biases residuals  $\mathbf{r}_\omega^m$ , and time-shift residuals  $r_t^m$ . That is

$$C(\mathcal{S}) = \sum_{a \in \mathcal{A}} \|d_a\|_{\Sigma_{d_a}}^2 + \sum_{m=0}^{M-1} \|r_t^m\|_{\Sigma_{r_t^m}}^2 + \sum_{m=1}^{M-1} \left( \|\mathbf{r}_f^m\|_{\Sigma_{r_f^m}}^2 + \|\mathbf{r}_\omega^m\|_{\Sigma_{r_\omega^m}}^2 + \|\mathbf{r}_f^m\|_{\Sigma_{r_f^m}}^2 \right). \quad (4)$$

The different components of  $C(\mathcal{S})$  are detailed in Section IV. Note that  $\Sigma_\bullet$  is the covariance matrix of the variable  $\bullet$ .

### C. Upsampled Preintegrated Measurement

The proposed framework uses UPMs to accurately address the problem of motion distortion in lidar scans. We previously introduced these measurements in [2] based on concepts originally presented in [3] and [4]. The original idea of preintegration [3] consists in reducing the size of the state to estimate by combining IMU measurements between two estimated poses. From acceleration and angular velocities, IMU readings are naturally combined through integration. Problem is, as per the physics definition of accelerometer readings, the integration is computed based on initial conditions, which become part of the estimated state. In such a configuration,

every modification of the state would require recomputation of all the integrals. Preintegration allows the computation of the integrals independently from the initial conditions. In other words, authors of [4] created a new type of measurements that remain constant during the estimation process and that links two consecutive poses of the state.

The original preintegrated measurements, as defined in [4], are

$$\begin{aligned} \Delta \mathbf{p}_{\tau_m}^{t_i} &= \sum_{k=\kappa}^{i-1} \left( \Delta \mathbf{v}_{\tau_m}^{t_k} \Delta t_k + \frac{1}{2} \Delta \mathbf{R}_{\tau_m}^{t_k} (\mathbf{f}(t_k - \delta_t^m) - \mathbf{b}_f^m) \Delta t_k^2 \right) \\ \Delta \mathbf{v}_{\tau_m}^{t_i} &= \sum_{k=\kappa}^{i-1} \Delta \mathbf{R}_{\tau_m}^{t_k} (\mathbf{f}(t_k - \delta_t^m) - \mathbf{b}_f^m) \Delta t_k \\ \Delta \mathbf{R}_{\tau_m}^{t_i} &= \prod_{k=\kappa}^{i-1} \operatorname{Exp}((\boldsymbol{\omega}(t_k - \delta_t^m) - \mathbf{b}_\omega^m) \Delta t_k), \end{aligned} \quad (5)$$

with  $\{\kappa \in \mathbb{N} | t_\kappa = \tau_m\}$ ,  $\Delta t_k = t_{k+1} - t_k$ , and  $\operatorname{Exp}(\cdot)$  the exponential mapping from the axis-angle representations ( $\mathfrak{so}(3)$ ) to rotation matrices ( $SO(3)$ ) defined as

$$\operatorname{Exp}(\boldsymbol{\phi}) = \mathbf{I} + \frac{\sin(\|\boldsymbol{\phi}\|)}{\|\boldsymbol{\phi}\|} \boldsymbol{\phi}^\wedge + \frac{1 - \cos(\|\boldsymbol{\phi}\|)}{\|\boldsymbol{\phi}\|^2} (\boldsymbol{\phi}^\wedge)^2, \quad (6)$$

$$\text{where } \boldsymbol{\phi}^\wedge = \begin{bmatrix} \phi_1 \\ \phi_2 \\ \phi_3 \end{bmatrix}^\wedge = \begin{bmatrix} 0 & -\phi_3 & \phi_2 \\ \phi_3 & 0 & -\phi_1 \\ -\phi_2 & \phi_1 & 0 \end{bmatrix}. \quad (7)$$

Then the pose and velocity of the IMU at time  $t_i$  are

$$\mathbf{p}_W^{t_i} = \mathbf{p}_W^{\tau_m} + \Delta \zeta_m^i \mathbf{v}_W^{\tau_m} + \frac{1}{2} \Delta \zeta_m^i{}^2 \mathbf{g} + \mathbf{R}_W^{\tau_m} \Delta \mathbf{p}_{\tau_m}^{t_i} \quad (8)$$

$$\mathbf{v}_W^{t_i} = \mathbf{v}_W^{\tau_m} + \Delta \zeta_m^i \mathbf{g} + \mathbf{R}_W^{\tau_m} \Delta \mathbf{v}_{\tau_m}^{t_i} \quad (9)$$

$$\mathbf{R}_W^{t_i} = \mathbf{R}_W^{\tau_m} \Delta \mathbf{R}_{\tau_m}^{t_i}, \quad (10)$$

where  $\mathbf{g}$  is the known gravity vector in  $\mathfrak{F}_W$  and  $\Delta \zeta_m^i = t_i - \tau_m$ .

The issue addressed by the UPMs is the general asynchronism between the IMU and any other sensor, both in terms of time-shift and difference of acquisition frequency. For the lidar-IMU pair, unlike in [3] and [4], the IMU is the low acquisition frequency sensor. With a rotating lidar moving in space, each of the points is collected from a different pose. To constrain the motion during a sweep, inertial data need to be available at each lidar point's timestamp. The key idea of UPMs is to compute a continuous representation of the inertial data to allow its estimation at any arbitrary timestamp and therefore enable the computation of preintegrated measurements for each lidar point.

Technically, given raw IMU readings  $\mathbf{f}_i$  and  $\boldsymbol{\omega}_i$ , GP regression [23] is used to probabilistically infer  $\mathbf{f}^*(t)$  and  $\boldsymbol{\omega}^*(t)$  at any time  $t$ . The use of a non-parametric interpolation methods make the UPMs independent of any explicit motion model. Multiple regressions are conducted independently for each IMU measurement DoF with constant mean functions and isometric Matern covariance functions.

Let us denote  $s_j$  the  $j^{\text{th}}$  DoF of the IMU readings to be interpolated. The mean and variance of  $s_j$  are computed as

$$s_j^*(t) = \mathbf{k}_*^\top (\mathbf{K} + \sigma_{s_j}^2 \mathbf{I})^{-1} \mathbf{s}_j, \text{ and} \quad (11)$$

$$\sigma_{s_j}^{*2}(t) = k(t, t) - \mathbf{k}_*^\top (\mathbf{K} + \sigma_{s_j}^2 \mathbf{I})^{-1} \mathbf{k}_*, \quad (12)$$



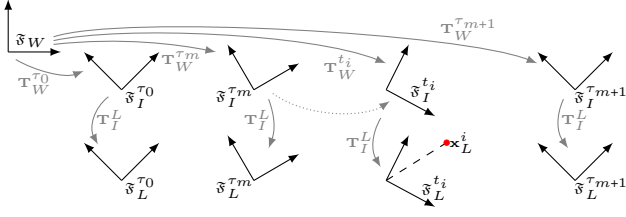


Fig. 4: Frames and frame transformations during a sequence of measurements.  $\mathfrak{F}_I^{\tau_m}$  and  $\mathfrak{F}_L^{\tau_m}$  respectively represent the IMU and lidar frames at time  $\tau_m$ . The gray continuous line arrows represent the transformations between the different frames.  $\mathfrak{F}_W$  is the world fixed frame. The dotted line shows the use of upsampled preintegrated measurements to reproject the point  $\mathbf{x}_L^i$ .

with  $\mathbf{s}_j$  being the corresponding vector of training values for  $s_j$ ,  $\mathbf{k}_*$  the cross-correlation between the new sample point  $t$  and the training samples at  $t_i$ ,  $\sigma_{s_j}^2$  the variance of the Gaussian noise of the training data,  $k(\cdot, \cdot)$  the kernel function, and  $\mathbf{K}$  the matrix of the covariances evaluated at all pairs of training samples.

To address the cubic complexity of the GP regression, GPs are trained with samples in temporal windows aligned with the lidar frame scanning time (from  $\tau_m$  to  $\tau_{m+1}$ ). More rigorously, to infer the IMU readings for each of the points in  $\mathcal{X}^m$ , training samples must have a timestamp  $t_i \in [\tau_m - o; \tau_{m+1} + o]$ , with  $o$  a time overlap over the adjacent frames. The hyperparameters of the Matern covariance function are optimised for each of the training windows.

#### IV. BACK-END

##### A. Lidar factors

Lidar factors correspond to distance residuals computed between lidar feature-points and their corresponding feature-points from other lidar frames. As we will explain in the front-end section, the set of feature associations  $\mathcal{A}$  contains tuples of 3 (point-to-edge constraints) or 4 feature-points (point-to-plane constraints).

For the lidar factors, point-to-line or point-to-plane distances are used. The matched points found in  $\mathcal{A}$  are projected in the world frame  $\mathfrak{F}_W$  using the calibration parameters, UPMs for each of the points and the current estimates of the IMU poses and velocities (Fig. 4). Therefore a point  $\mathbf{x}_L^i \in \mathcal{X}^m$  is projected in  $\mathfrak{F}_W$  using (2), (8) and (10),

$$\begin{bmatrix} \mathbf{x}_W^i \\ 1 \end{bmatrix} = \mathbf{T}_W^{t_i} \mathbf{T}_I^L \begin{bmatrix} \mathbf{x}_L^i \\ 1 \end{bmatrix}. \quad (13)$$

Let us denote an edge association  $\mathbf{a}_3 \in \mathcal{A}$ .  $\mathbf{a}_3 = \{\mathbf{x}_L^i, \mathbf{x}_L^j, \mathbf{x}_L^k\}$  with  $\mathbf{x}_L^i \in \mathcal{F}^m$ ,  $\mathbf{x}_L^j \in \mathcal{F}^n$ ,  $\mathbf{x}_L^k \in \mathcal{F}^o$  and  $n, o \neq m$ . These points are projected in  $\mathfrak{F}_W$  via (13) to get  $\mathbf{x}_W^i$ ,  $\mathbf{x}_W^j$  and  $\mathbf{x}_W^k$ . The point-to-line distance

$$d_{\mathbf{a}_3} = \frac{\|(\mathbf{x}_W^i - \mathbf{x}_W^j) \times (\mathbf{x}_W^i - \mathbf{x}_W^k)\|_2}{\|(\mathbf{x}_W^j - \mathbf{x}_W^k)\|_2} \quad (14)$$

is used as an edge feature residual.

Let us denote a plane association  $\mathbf{a}_4 \in \mathcal{A}$ .  $\mathbf{a}_4 = \{\mathbf{x}_L^i, \mathbf{x}_L^j, \mathbf{x}_L^k, \mathbf{x}_L^l\}$  with  $\mathbf{x}_L^i \in \mathcal{F}^m$ ,  $\mathbf{x}_L^j \in \mathcal{F}^n$ ,  $\mathbf{x}_L^k \in \mathcal{F}^o$ ,  $\mathbf{x}_L^l \in \mathcal{F}^p$  and  $n, o, p \neq m$ . These points are projected in  $\mathfrak{F}_W$  via (13) to get  $\mathbf{x}_W^i$ ,  $\mathbf{x}_W^j$ ,  $\mathbf{x}_W^k$  and  $\mathbf{x}_W^l$ . The point-to-plane distance

$$d_{\mathbf{a}_4} = \frac{(\mathbf{x}_W^i - \mathbf{x}_W^j)^\top ((\mathbf{x}_W^j - \mathbf{x}_W^k) \times (\mathbf{x}_W^j - \mathbf{x}_W^l))}{\|(\mathbf{x}_W^j - \mathbf{x}_W^k) \times (\mathbf{x}_W^j - \mathbf{x}_W^l)\|_2} \quad (15)$$

is used as a plane feature residual. As in [2], the variance of lidar residuals requires the knowledge of the state. Therefore, the noise propagation needs to be executed regularly during the optimisation.

##### B. IMU factors

The IMU factors constitute direct constraints on the IMU poses and velocities. The associated residual  $\mathbf{r}_I^m = [\mathbf{r}_{I_r}^m; \mathbf{r}_{I_v}^m; \mathbf{r}_{I_p}^m]$  is obtained directly by manipulating (8), (9), and (10),

$$\begin{aligned} \mathbf{r}_{I_p}^m &= \mathbf{R}_W^{\tau_m \top} (\mathbf{p}_W^{\tau_{m+1}} - \mathbf{p}_W^{\tau_m} - \Delta\tau_m \mathbf{v}_W^{\tau_m} - \frac{\Delta\tau_m^2}{2} \mathbf{g}) - \Delta\mathbf{p}_{\tau_m}^{\tau_{m+1}} \\ \mathbf{r}_{I_v}^m &= \mathbf{R}_W^{\tau_m \top} (\mathbf{v}_W^{\tau_{m+1}} - \mathbf{v}_W^{\tau_m} - \Delta\tau_m \mathbf{g}) - \Delta\mathbf{v}_{\tau_m}^{\tau_{m+1}} \\ \mathbf{r}_{I_r}^m &= \text{Log}(\Delta\mathbf{R}_{\tau_m}^{\tau_{m+1} \top} \mathbf{R}_W^{\tau_m \top} \mathbf{R}_W^{\tau_{m+1}}), \end{aligned} \quad (16)$$

with  $\Delta\tau_m = \tau_{m+1} - \tau_m$ .

##### C. IMU biases and inter-sensor time-shift

The UPMs computation (5) is a function of the accelerometer biases  $\mathbf{b}_f$ , gyroscope biases  $\mathbf{b}_\omega$ , and inter-sensor time-shift  $\delta_t$ . Unfortunately these values are not perfectly known at the time of preintegration. In our framework, we modelled the IMU biases as a Brownian motion as in [20] and the inter-sensor time-shift as a simple Gaussian. By considering biases and time-shift locally constant during lidar frames, and by adopting a first-order expansion as in [4], the UPMs can be approximated as follow:

$$\begin{aligned} \Delta\mathbf{R}_{\tau_m}^{t_i}(\mathbf{b}_\omega, \delta_t) &\approx \Delta\mathbf{R}_{\tau_m}^{t_i}(\bar{\mathbf{b}}_\omega^m, \bar{\delta}_t^m) \text{Exp} \left( \frac{\partial \Delta\mathbf{R}_{\tau_m}^{t_i}}{\partial \mathbf{b}_\omega} \hat{\mathbf{b}}_\omega^m + \frac{\partial \Delta\mathbf{R}_{\tau_m}^{t_i}}{\partial \delta_t} \hat{\delta}_t^m \right) \\ \Delta\mathbf{v}_{\tau_m}^{t_i}(\mathbf{b}_f, \mathbf{b}_\omega, \delta_t) &\approx \Delta\mathbf{v}_{\tau_m}^{t_i}(\bar{\mathbf{b}}_f^m, \bar{\mathbf{b}}_\omega^m, \bar{\delta}_t^m) + \frac{\partial \Delta\mathbf{v}_{\tau_m}^{t_i}}{\partial \mathbf{b}_f} \hat{\mathbf{b}}_f^m + \frac{\partial \Delta\mathbf{v}_{\tau_m}^{t_i}}{\partial \mathbf{b}_\omega} \hat{\mathbf{b}}_\omega^m + \frac{\partial \Delta\mathbf{v}_{\tau_m}^{t_i}}{\partial \delta_t} \hat{\delta}_t^m \\ \Delta\mathbf{p}_{\tau_m}^{t_i}(\mathbf{b}_f, \mathbf{b}_\omega, \delta_t) &\approx \Delta\mathbf{p}_{\tau_m}^{t_i}(\bar{\mathbf{b}}_f^m, \bar{\mathbf{b}}_\omega^m, \bar{\delta}_t^m) + \frac{\partial \Delta\mathbf{p}_{\tau_m}^{t_i}}{\partial \mathbf{b}_f} \hat{\mathbf{b}}_f^m + \frac{\partial \Delta\mathbf{p}_{\tau_m}^{t_i}}{\partial \mathbf{b}_\omega} \hat{\mathbf{b}}_\omega^m + \frac{\partial \Delta\mathbf{p}_{\tau_m}^{t_i}}{\partial \delta_t} \hat{\delta}_t^m, \end{aligned} \quad (17)$$

with  $\mathbf{b}_f^m = \bar{\mathbf{b}}_f^m + \hat{\mathbf{b}}_f^m$ ,  $\mathbf{b}_\omega^m = \bar{\mathbf{b}}_\omega^m + \hat{\mathbf{b}}_\omega^m$ , and  $\delta_t^m = \bar{\delta}_t^m + \hat{\delta}_t^m$ . Note that  $\bar{\bullet}$  denotes the prior knowledge of the value at the

time of preintegration and  $\hat{\bullet}$  represents the correction. The residuals

$$\mathbf{r}_f^m = \bar{\mathbf{b}}_f^m + \hat{\mathbf{b}}_f^m - \bar{\mathbf{b}}_f^{m-1} - \hat{\mathbf{b}}_f^{m-1} \quad (18)$$

$$\mathbf{r}_\omega^m = \bar{\mathbf{b}}_\omega^m + \hat{\mathbf{b}}_\omega^m - \bar{\mathbf{b}}_\omega^{m-1} - \hat{\mathbf{b}}_\omega^{m-1} \quad (19)$$

are used in the biases factors to impose the Brownian motion constraint. The time-shift factor residual is simply  $r_t^m = \hat{\delta}_t^m$  as per the Gaussian noise model.

## V. FRONT-END

The front-end of the proposed method aims at populating the set  $\mathcal{A}$  of lidar feature-point associations to allow frame-to-frame and loop closure matching.

### A. Feature extraction

This section of the proposed method has been described in the conference paper [5], but for completeness it is also described here with additional details.

The vertical resolution of most of today's lidars has driven the design of our feature extraction algorithm toward a channel-by-channel method in a similar way to the one in [10]. The authors of [10] introduced a computationally efficient smoothness score for feature extraction/classification. While robust in weakly structured environments and allowing real-time operations, this score computation is not fully consistent. For example, points belonging to the same planar surface will have different smoothness scores despite the same underlying structure. We propose a feature extraction technique based on linear regression to consistently describe the surface observed by the lidar.

Given an N-channel lidar, each lidar scan  $\mathcal{X}^m$  is split into  $N$  "lines",  $\mathcal{N}_l^m$  ( $l = 1, \dots, N$ ), according to the elevation of the 3D-points collected. All the points are given a curvature score. The curvature computation aims at fitting lines to two subsets of points adjacent to the point under examination  $\mathbf{x}_L^i \in \mathcal{N}_l^m$ , and then to retrieve the cosine of the angle between these two lines. The subsets,  $\mathcal{L}_i$  and  $\mathcal{R}_i$  contain the  $D$  previous and following measurements (to  $\mathbf{x}_L^i$ ) in  $\mathcal{N}_l^m$ .

First, the points need to be reprojected into the lidar frame at  $\tau_m$  ( $\mathcal{F}_L^{\tau_m}$ ) to remove motion distortion according to the best current estimate of the state  $\mathcal{S}$ . These reprojected points  $\mathbf{x}_{L_m}^i$  are computed as follow:

$$\begin{bmatrix} \mathbf{x}_{L_m}^i \\ 1 \end{bmatrix} = (\mathbf{T}_I^L)^{-1} (\mathbf{T}_W^{\tau_m})^{-1} \mathbf{T}_W^{t_i} \mathbf{T}_I^L \begin{bmatrix} \mathbf{x}_L^i \\ 1 \end{bmatrix}. \quad (20)$$

The curvature scores are computed under the approximation that around a certain azimuth the consecutively measured 3D-points belong to the same plane. As shown in Fig. 5, and given  $\alpha^i$  the new azimuth of  $\mathbf{x}_{L_m}^i$ , the points in  $\mathcal{L}_i$  and  $\mathcal{R}_i$  are projected on a plane space around  $\alpha^i$

$$x_{P_i}^k = |\mathbf{x}_{L_m}^{i+k}| \sin(\alpha^{i+k} - \alpha^i), \quad (21)$$

$$y_{P_i}^k = |\mathbf{x}_{L_m}^{i+k}| \cos(\alpha^{i+k} - \alpha^i), \quad (22)$$

with  $k = -D, \dots, D$ .

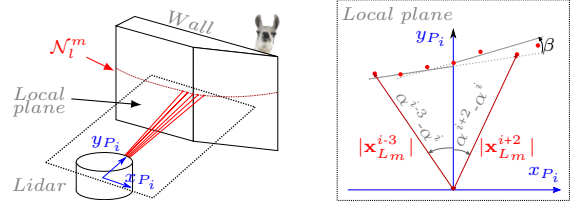


Fig. 5: Geometric feature extraction based on linear regression. The points around a given azimuth are assumed to belong to a local plane. On that local plane, linear regressions are performed considering points in  $\mathcal{N}_l^m$  on both sides of the  $i^{th}$  point  $\mathbf{x}_L^i \in \mathcal{N}_l^m$  independently. The curvature score is equal to  $\cos(\beta)$  with  $\beta$  the angle between the two fitted lines.

$$\mathbf{X}_{\mathcal{L}_i} = \begin{bmatrix} 1 & x_{P_i}^{-D} \\ \vdots & \vdots \\ 1 & x_{P_i}^0 \end{bmatrix}, \mathbf{X}_{\mathcal{R}_i} = \begin{bmatrix} 1 & x_{P_i}^0 \\ \vdots & \vdots \\ 1 & x_{P_i}^D \end{bmatrix}, \quad (23)$$

$$\mathbf{Y}_{\mathcal{L}_i} = [y_{P_i}^{-D} \cdots y_{P_i}^0]^\top \text{ and } \mathbf{Y}_{\mathcal{R}_i} = [y_{P_i}^0 \cdots y_{P_i}^D]^\top$$

group the projected points coordinates according to the two adjacent subsets  $\mathcal{L}_i$  and  $\mathcal{R}_i$ . In the rest of this section,  $\bullet$  represents either  $\mathcal{L}_i$  or  $\mathcal{R}_i$ . A line of slope  $s_\bullet$  and y-intercept  $q_\bullet$  can be fitted to the subset  $\bullet$  with

$$[q_\bullet \quad s_\bullet]^\top = (\mathbf{X}_\bullet^\top \mathbf{X}_\bullet)^{-1} \mathbf{X}_\bullet^\top \mathbf{Y}_\bullet, \quad (24)$$

and an associated unit direction vector can be obtained as

$$\mathbf{v}_\bullet = \begin{bmatrix} \frac{1}{\sqrt{1+s_\bullet^2}} & \frac{s_\bullet}{\sqrt{1+s_\bullet^2}} \end{bmatrix}^\top. \quad (25)$$

The regression error values

$$\bar{e}_\bullet^i = \frac{1}{|\bullet|} \sum_{k|\mathbf{x}_L^k \in \bullet} |y_{P_i}^k - q_\bullet - s_\bullet x_{P_i}^k| \quad (26)$$

$$e_\bullet^i = \max_{k|\mathbf{x}_L^k \in \bullet} (|y_{P_i}^k - q_\bullet - s_\bullet x_{P_i}^k|) \quad (27)$$

are used to reject points or to detect border of occlusions as per Algorithm 1. The score  $c_i = \mathbf{v}_{\mathcal{L}_i}^\top \mathbf{v}_{\mathcal{R}_i}$  represents the cosine of the angle between the two fitted lines. As a consequence,  $c_i$  is close to 1 when the underlying surface is planar and decreases with the sharpness of edges.

As in [10], surfaces close to being parallel to the laser beams are rejected as features. We also use a system of bins and a maximum number of features per bin on each laser line to ensure the features are spread over the whole scan. The points with the highest scores in each of the bins of  $\mathcal{N}_l^m$  are classified as planar points and the lowest scores as edges according to arbitrarily chosen maximum numbers of features per bin and thresholds on scores. The edge orientation, inward (pointing toward the lidar) or outward (point away from the lidar), can be defined by looking at the values of the regressed lines' parameters. All the planar features in  $\mathcal{N}_l^m$  with  $l = 1, \dots, N$ , are grouped into a set  $\mathcal{P}^m$ , the inward edges in  $\mathcal{E}_I^m$  and outward edges in  $\mathcal{E}_O^m$ . The reader should note that the feature set (from the back-end section of this paper)  $\mathcal{F}^m = \mathcal{P}^m \cup \mathcal{E}_I^m \cup \mathcal{E}_O^m$ .

---

**Algorithm 1** Rejection of lidar points as potential feature according to linear regression errors
 

---

**Input:**

$\bar{e}_{th}$ : Threshold on mean regression error  
 $e_{th}$ : Threshold on max regression error  
 $\bar{e}_{\mathcal{L}}^i, \bar{e}_{\mathcal{R}}^i, e_{\mathcal{L}}^i, e_{\mathcal{R}}^i$ : Regression errors in  $\mathcal{L}_i$  and  $\mathcal{R}_i$

**Output:**

*Point\_rejected*: Boolean flag to prevent point of being feature

*Point\_rejected*  $\leftarrow$  false

**if**  $(\bar{e}_{\mathcal{L}}^i < \bar{e}_{th}) \text{ and } (e_{\mathcal{L}}^i < e_{th}) \text{ and } (\bar{e}_{\mathcal{R}}^i < \bar{e}_{th}) \text{ and } (e_{\mathcal{R}}^i < e_{th})$  **then**  
 // Good regression

return

**else if**  $((\bar{e}_{\mathcal{L}}^i > \bar{e}_{th}) \text{ or } (e_{\mathcal{L}}^i > e_{th})) \text{ and } ((\bar{e}_{\mathcal{R}}^i > \bar{e}_{th}) \text{ or } (e_{\mathcal{R}}^i > e_{th}))$  **then**  
 // None of the regression is reliable

*Point\_rejected*  $\leftarrow$  true

**else**

**if**  $(\bar{e}_{\mathcal{L}}^i < \bar{e}_{th}) \text{ and } (e_{\mathcal{L}}^i < e_{th})$  **then**

// Left regression OK, border of occlusion ?

Recompute  $\bar{e}_{\mathcal{R}}^i$  and  $e_{\mathcal{R}}^i$  based on  $\mathcal{R}_i \setminus \mathbf{x}_{\mathcal{L}}^i$

**if**  $(\bar{e}_{\mathcal{R}}^i > \bar{e}_{th}) \text{ or } (e_{\mathcal{R}}^i > e_{th}) \text{ or } (s_{\mathcal{R}_i} x_{P_i}^1 + q_{\mathcal{R}_i} < |\mathbf{x}_{\mathcal{L}_m}^i|)$  **then**  
 // Right regression not reliable or border of occlusion

*Point\_rejected*  $\leftarrow$  true

**else**

$s_{\mathcal{R}_i} \leftarrow (y_{P_i}^1 - y_{P_i}^0) / (x_{P_i}^1 - x_{P_i}^0)$  and recompute  $\mathbf{v}_{\mathcal{R}_i}$

**end if**

**else if**  $(\bar{e}_{\mathcal{R}}^i < \bar{e}_{th}) \text{ and } (e_{\mathcal{R}}^i < e_{th})$  **then**

// Right regression OK, border of occlusion ?

Recompute  $\bar{e}_{\mathcal{L}}^i$  and  $e_{\mathcal{L}}^i$  based on  $\mathcal{L}_i \setminus \mathbf{x}_{\mathcal{L}}^i$

**if**  $(\bar{e}_{\mathcal{L}}^i > \bar{e}_{th}) \text{ or } (e_{\mathcal{L}}^i > e_{th}) \text{ or } (s_{\mathcal{L}_i} x_{P_i}^{-1} + q_{\mathcal{L}_i} < |\mathbf{x}_{\mathcal{L}_m}^i|)$  **then**  
 // Left regression not reliable or border of occlusion

*Point\_rejected*  $\leftarrow$  true

**else**

$s_{\mathcal{L}_i} \leftarrow (y_{P_i}^0 - y_{P_i}^{-1}) / (x_{P_i}^0 - x_{P_i}^{-1})$  and recompute  $\mathbf{v}_{\mathcal{L}_i}$

**end if****else**

*Point\_rejected*  $\leftarrow$  true

**end if****end if**


---

**B. Feature recomputation**

The aforementioned process of feature extraction is computationally costly and depends on the last estimate of the state  $\mathcal{S}$ . IN2LAAMA integrates a way to check the validity of features without the need to recompute all the linear regressions.

For the moment, let us consider planar features only and define  $N_f$  as the maximum number of planar features selected per bin during the feature extraction performed on the  $m^{\text{th}}$  lidar frame. The set of planar features in the  $k^{\text{th}}$  bin of the  $m^{\text{th}}$  lidar frame is noted  $\mathcal{B}_{m,k}^j$  with  $j > 0$  corresponding to the  $j^{\text{th}}$  time the features of frame  $m$  have been computed. Considering the case  $j = 1$ , the scores  $c_i$  are computed for all points in  $\mathcal{X}^m$ . The points are then sorted according to their score in a decreasing order. Starting from the highest score, points are added to  $\mathcal{B}_{m,k}^j$  if their score is above a threshold and as long as  $|\mathcal{B}_{m,k}^j| < N_f$ . The algorithm also stores the  $N_f$  next candidates (even if they do not match the threshold) in the set  $\mathcal{C}_{m,k}^j$ . Note that the set union of the planar feature bins  $\mathcal{B}_{m,k}^j$  is  $\mathcal{P}^m$ .

In the case of  $j > 1$ , typically after an optimisation iteration of the factor graph the state  $\mathcal{S}$  changes. The features potentially

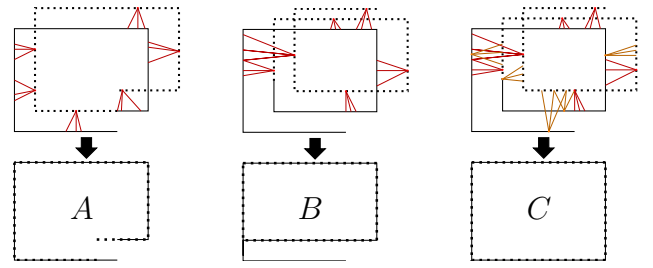


Fig. 6: Different data association strategies between a scan  $\mathcal{X}^m$  (dashed line) and its previous scan  $\mathcal{X}^{m-1}$  (plain line). The top row represents the data association. The bottom is the results after minimising point-to-plane distances. *A* uses 360° scans with back-association. *B* uses scans greater than 360°, with back-association. *C* extends *B* with back-and-forth-association. *C* ensure consistency of the lidar scans whereas *A* and *B* do not.

need to be recomputed. The score of the points in  $\mathcal{B}_{m,k}^{j-1}$  and  $\mathcal{C}_{m,k}^{j-1}$  are recomputed and sorted by decreasing order. The point selection for the bins is done as if  $j = 1$  but using point scores from  $\mathcal{B}_{m,k}^{j-1} \cup \mathcal{C}_{m,k}^{j-1}$  and not from  $\mathcal{X}^m$ . An overlap ratio of number of features is computed as per

$$\Theta_{j,m} = \frac{\left| \left( \bigcup_k \mathcal{B}_{m,k}^j \right) \cap \left( \bigcup_k \mathcal{B}_{m,k}^{j-1} \right) \right|}{\left| \left( \bigcup_k \mathcal{B}_{m,k}^{j-1} \right) \right|}. \quad (28)$$

If  $\Theta_{j,m}$  is close to one then  $\mathcal{B}_{m,k}^j \leftarrow \mathcal{B}_{m,k}^{j-1}$  and  $\mathcal{C}_{m,k}^j \leftarrow \mathcal{C}_{m,k}^{j-1}$ . Otherwise,  $\mathcal{B}_{m,k}^j$  and  $\mathcal{C}_{m,k}^j$  are recomputed from  $\mathcal{X}^m$  as per the case  $j = 1$ . Similar process is used when edge features are also used.

**C. Data association**

The proposed scan registration method requires matching features from frame-to-frame. Feature matching is usually prone to outliers, thus a robust process for data association is needed. This section describes the different processes used in IN2LAAMA for matching and outlier rejection.

1) *Feature matching*: For a pair of lidar frames  $i$  and  $m$ , after reprojecting both frames into  $\mathbb{F}_W$  and for each point of  $\mathcal{P}^i$ , the method looks for the 3 nearest neighbours in  $\mathcal{P}^m$ . For points in  $\mathcal{E}_I^i$  and  $\mathcal{E}_O^i$ , only the 2 nearest neighbours are searched in  $\mathcal{E}_I^m$  and  $\mathcal{E}_O^m$  respectively. In both cases, to limit the impact of the measurements' noise on the point-to-line and point-to-plane distances used as lidar residuals, the  $n = \{2, 3\}$  closest points need to be spatially spread over some minimum distances. The  $n$  closest points cannot belong to a single lidar channel. If the  $n$  closest points do not satisfy these conditions, the subsequent closest points are considered. For planar feature associations, the collinearity of the 3 points from  $\mathcal{P}^m$  is checked. Kd-trees [24] are used for efficient nearest neighbour searches. The data associations are included in  $\mathcal{A}$  as tuples of 3 or 4 as per the type of feature.

To ensure lidar scans' consistency, the proposed method considers scans greater than 360° (520° in our implementation) and do the data association both from  $i$  to  $m$ , and from

$m$  to  $i$ . The idea behind these choices is illustrated in Fig. 6 through a 2D example where a lidar moves in a rectangular room detecting only planar features. In the scenario A, the data association between scans of  $360^\circ$  (or less) does not allow the correction of the motion distortion in the scans. In the scenario B, the scans are greater than  $360^\circ$  but the lower wall of the first scan does not appear in any data association. The scenario C fully constrains the scan consistency correcting the motion distortion by having both scans greater than  $360^\circ$  combined with back-and-forth data association.

Intuitively the greater the angle swept by a scan is, the better the scan consistency is, but there is a trade-off with the execution time. The UPMs' GP regressions are computed from the IMU readings that are collected during a lidar scan. Therefore, larger lidar scans imply cubically longer inference time as per the  $\mathcal{O}(n^3)$  complexity of GP interpolation.

2) *Outliers rejection*: To remove outliers from  $\mathcal{A}$ , matching points spread over too large areas are disregarded. For planar features, a more robust outlier detection is implemented by analysing the patch around the matched feature-points. Considering a planar point  $\mathbf{x}_W^i$  associated with  $\mathbf{x}_W^j$ ,  $\mathbf{x}_W^k$ , and  $\mathbf{x}_W^l$ , the line-neighbours of each of the 3 matched points from  $\mathcal{P}^m$  ( $\mathcal{L}_j$ ,  $\mathcal{R}_j$ ,  $\mathcal{L}_k$ ,  $\mathcal{R}_k$ ,  $\mathcal{L}_l$ , and  $\mathcal{R}_l$ ) are placed in a set  $\mathcal{U}$ . If the points in  $\mathcal{U}$  do not belong to the plane described by  $\mathbf{x}_W^j$ ,  $\mathbf{x}_W^k$ , and  $\mathbf{x}_W^l$ , the association is rejected. Formally, an association is valid if

$$\max_{\mathbf{x}_W^u \in \mathcal{U}} \left( \frac{(\mathbf{x}_W^u - \mathbf{x}_W^j)^\top ((\mathbf{x}_W^j - \mathbf{x}_W^k) \times (\mathbf{x}_W^j - \mathbf{x}_W^l))}{\|(\mathbf{x}_W^j - \mathbf{x}_W^k) \times (\mathbf{x}_W^j - \mathbf{x}_W^l)\|_2} \right) \quad (29)$$

complies with the lidar range noise.

In cluttered environment, it is still likely that some outliers pass the aforementioned tests. Thus, a Cauchy loss function is applied to the lidar residuals in order to attenuate the impact of the potential remaining outliers on the optimisation.

#### D. Loop-closure detection

Loop-closures allow localisation and mapping algorithms to correct the accumulated drift inherent to frame-to-frame trajectory estimation. In the proposed method, loop-closures are modelled with additional lidar factors as shown in Fig. 3.

A simple geometric loop-closure detection based on estimated poses proximity has been implemented. In other words, if two poses are close enough, a lidar factor is built between these two poses (performing feature matching and adding a set of residuals to the cost functions). An optional ICP test is conducted to validate the loop closure.

Commonly used lidars have a  $360^\circ$  field-of-view around the spinning axis (azimuth) but have a narrower angular range on the other axis (elevation). The nature of that setup results in big overlaps between scans that have been collected while the lidar rotates around its spinning axis. On the other hand, if the lidar rotates around other axes, the geometric data overlap decreases, making the registration between two scans more challenging. Therefore, the direct angle between two orientations cannot be used as part of the proximity metric. The  $360^\circ$  "horizontal" field-of-view of the lidar must be taken into account.

Let us consider a spinning lidar that sweeps the environment around the z-axis of its reference frame. The origin of the frame coincides with the lidar optical centre. The different metrics used to define the closeness between two lidar frames  $\mathfrak{F}_L^{\tau_m}$  and  $\mathfrak{F}_L^{\tau_i}$  are as follow:

- $d_r$  is the radial distance of the origin of  $\mathfrak{F}_L^{\tau_i}$  regarding the z-axis of  $\mathfrak{F}_L^{\tau_m}$ .
- $d_h$  is the point-to-plane distance between the origin of  $\mathfrak{F}_L^{\tau_i}$  and the plane formed by the x and y axes of  $\mathfrak{F}_L^{\tau_m}$ .
- $d_\alpha$  is the angle between the z-axes  $\mathfrak{F}_L^{\tau_i}$  and  $\mathfrak{F}_L^{\tau_m}$  when their origins coincide.

More formally,

$$d_r = \sqrt{x_m^i{}^2 + y_m^i{}^2} \quad (30)$$

$$d_h = |z_m^i| \quad (31)$$

$$\cos(d_\alpha) = \mathbf{u}_z^\top \mathbf{R}_I^L \mathbf{R}_W^{\tau_m \top} \mathbf{R}_W^{\tau_i} \mathbf{R}_I^L \mathbf{u}_z, \quad (32)$$

with  $\begin{bmatrix} x_m^i & y_m^i & z_m^i & 1 \end{bmatrix}^\top = (\mathbf{T}_I^L)^{-1} (\mathbf{T}_W^{\tau_m})^{-1} \mathbf{T}_W^{\tau_i} \begin{bmatrix} \mathbf{p}_I^L \\ 1 \end{bmatrix}$

and  $\mathbf{u}_z = \begin{bmatrix} 0 & 0 & 1 \end{bmatrix}^\top$ .

To limit the amount of redundant loop-closures, IN2LAAMA sets a minimum time between two consecutive loop-closures as well as a minimum gap time between the two frames used for closures. The algorithm looks for loop-closures every time a new frame is added to the factor graph. The metrics  $d_r$ ,  $d_h$ , and  $|\cos(d_\alpha)|$  are computed between this new frame and the previous frames, that satisfy the afore mentioned time conditions, by order of increasing timestamp. The first frame that complies with thresholds on the above metrics is considered as a valid loop-closure candidate. Optionally, a standard ICP [7] is conducted between the new frame and frames contained in a time window around the loop-closure candidate. In this case, the loop-closure is validated only if the ICP fitness score is below a given value. The validation of a loop-closure leads to the addition of a new lidar factor in the factor graph as it can be seen in Fig. 3.

## VI. ON THE FACTOR GRAPH AND IMPLEMENTATION

### A. Localisation and mapping factor graph

In the absence of trajectory and velocity priors (*no* GPS, *no* odometry, etc.), the factor graph used for state estimation is built iteratively and optimised as new factors are added to the cost function. Algorithm 2 shows the proposed strategy. Intuitively, the first frames need particular attention as per the initial state is completely unknown when the system is switched on. Therefore, during the initialisation step, the integration of any single new frame triggers all, the optimisation of the state  $\mathcal{S}$ , the feature recomputation and data association for *every* frame already in the graph. Once this initialisation step is finished, motion-distortion has been removed from the corresponding lidar scans. Feature recomputation in these frames is not needed later in the process (the features are reliable as computed on distortion-free lidar scans). Only the latest frames have their features and data association recomputed as the state  $\mathcal{S}$  changes. Note that the method still considers motion distortion in *all* the frames at all times because UPMs



are used in the lidar residuals, and the full trajectory is part of the state  $\mathcal{S}$ . Integrating IN2LAAMA into a more complex system that provides reliable prior information (e.g. a robotic platform with odometry, GPS in outdoor scenarios, etc.), could reduce significantly the number of iterations needed to build the factor graph (potentially in one go). The execution time would be greatly reduced in this case.

---

**Algorithm 2** Factor graph construction and optimisation procedure
 

---

**Input:**

$M$ : Number of frames in the dataset  
 $N_g$ : Number of frames to initialise initial conditions  
 $N_e$ : Number of frames added between each optimisation  
 $N_i$ : Max number optimisation iterations  
 $Calib$ : Activate calibration parameters estimation  
 $\Delta S_{thr}$ : State change threshold

**Output:**

$\mathcal{S}$ : State estimate

```

// Initialisation
 $F \leftarrow$  Create empty factor graph
for  $n = 0 : N_g - 1$  do
  Add frame  $n$  and associated factors to  $F$ 
   $i \leftarrow 1$ 
  repeat
     $i \leftarrow i + 1$  and  $\mathcal{S}_{prev} \leftarrow \mathcal{S}$ 
     $\mathcal{S} \leftarrow \text{Optimise}(F)$ 
    Check/recompute features in frames 0 to  $n$ 
  until  $i > N_i$  or  $(\mathcal{S} - \mathcal{S}_{prev}) < \Delta S_{thr}$ 
end for
if  $Calib$  then
   $N \leftarrow 1$ 
else
   $N \leftarrow N_e$ 
end if
// End initialisation

for  $n = N_g : M - 1$  do
  Add frame  $n$  and associated factors to  $F$ 
  if  $n \bmod N = 0$  or  $n = M - 1$  then
     $i \leftarrow 1$ 
    repeat
       $i \leftarrow i + 1$  and  $\mathcal{S}_{prev} \leftarrow \mathcal{S}$ 
       $\mathcal{S} \leftarrow \text{Optimise}(F)$ 
      Check/recompute features in frames  $n - N_e$  to  $n$ 
    until  $i > N_i$  or  $(\mathcal{S} - \mathcal{S}_{prev}) < \Delta S_{thr}$ 
  end if
  Check loop-closure and  $\mathcal{S} \leftarrow \text{Optimise}(F)$  if loop detected
end for
if  $Calib$  then
  Add  $\mathbf{T}_I^L$  to  $\mathcal{S}$  and  $i \leftarrow 1$ 
  repeat
     $i \leftarrow i + 1$  and  $\mathcal{S}_{prev} \leftarrow \mathcal{S}$ 
     $\mathcal{S} \leftarrow \text{Optimise}(F)$ 
    Check/recompute features in frames 0 to  $M - 1$ 
  until  $i > N_i$  or  $(\mathcal{S} - \mathcal{S}_{prev}) < \Delta S_{thr}$ 
end if

```

---

### B. Calibration factor graph

The localisation and mapping procedure relies on a good knowledge of  $\mathbf{T}_I^L$ . Using inaccurate calibration parameters can lead to contradicting information in the factor graph. As a consequence, using the integration of inertial data from the last

estimate of the state provide a prior that drift rapidly. For the autocalibration procedure, IN2LAAMA runs the localisation and mapping procedure based on any prior knowledge of  $\mathbf{T}_I^L$ , while performing the optimisation step every time a new frame is added to the factor graph (cf.  $N \leftarrow 1$  in Algorithm 2). Once the full trajectory is estimated based on the inaccurate calibration parameters, the calibration parameters  $\mathbf{T}_I^L$  are included as part of the state  $\mathcal{S}$  to be estimated along with the different poses, velocities, and bias and time-shift corrections already in  $\mathcal{S}$ . Given this new  $\mathcal{S}$ , the proposed method iteratively optimises the factor graph and recomputes features until the estimate converges.

### C. Factor balance

Our approach models sensor readings with additive zero-mean Gaussian noise, and IMU biases with Brownian motion using noise parameters specified by the manufacturers. These considerations might not capture the reality accurately. Similarly, using inaccurate extrinsic calibration parameters creates a gap between reality and the noise models used. These issues can create contradicting information in the estimation process.

In our previous work [2], we have shown that the global weight of the lidar factors in the optimisation depends on the arbitrarily set number of features used per frame. This chosen number does not necessarily represent the correct confidence of the lidar registration.

In this current work, we have implemented a weighting mechanism to individually cap overconfident IMU factors with respect to their corresponding lidar factors. We chose to limit the information disparity by capping the IMU-lidar weight ratio as

$$\Sigma_{\mathbf{r}_I^m}^{-1} \leftarrow \rho_m \frac{\sum_{\mathbf{a} \in \mathcal{A}_m} \Sigma_{d_a}^{-1}}{\text{tr}(\Sigma_{\mathbf{r}_I^m}^{-1})} \Sigma_{\mathbf{r}_I^m}^{-1} \quad (33)$$

$$\text{with } \rho_m = \min \left( \frac{\text{tr}(\Sigma_{\mathbf{r}_I^m}^{-1})}{\sum_{\mathbf{a} \in \mathcal{A}_m} \Sigma_{d_a}^{-1}}, \eta \right), \quad (34)$$

where  $\mathcal{A}_m$  is the set of lidar constraints between  $\mathcal{F}^m$  and  $\mathcal{F}^{m+1}$ , and  $\eta$  the capping ratio between IMU and lidar factors. Note that the number of lidar features used is taken into account through the summation in  $\mathcal{A}_m$ . Section VII-B provides an analysis of the impact of this capping ratio in different scenarios.

### D. Bias observability

The inertial navigation community have studied previously the observability of IMU biases in different estimation frameworks [25], [26], [27]. It has been proven that in the presence of inertial data, the biases of the accelerometer are observable only if the attitude of the system is perfectly known or if the trajectory contains rotations [28]. If none of this conditions is satisfied, the estimated state  $\mathcal{S}$  is not unique. In the case of lidar-inertial fusion, a lidar alone cannot provide an accurate global attitude without relying on strong heuristics that are not desired in generic localisation and mapping frameworks (e.g. Manhattan world with walls aligned with gravity vector). Therefore, an extra constraint is needed to tackle the

problem of translation-only trajectories. The proposed method overcomes this problem by integrating a simple factor that penalises the distance between the estimated accelerometer biases and the null vector.

This additional factor on  $\hat{\mathbf{b}}_f^0$  is added to the factor graph upon creation. Once the final frame's factors are added to the factor graph, the observability constraint is released (weigh null) and the cost function is minimised. If the magnitude of the accelerometer biases is far from zero, the constraint is re-established and the optimisation run again. This strategy covers the scenarios where the estimation ambiguity is present only at the start of the trajectory. Note that in the non-observable cases, the estimated biases and global orientation are inaccurate but the trajectory, therefore the map, is still consistent.

#### E. UPMs and memory

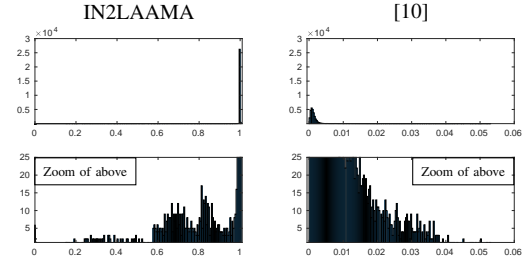
The main attribute of the UPMs is to make precise inertial data available for each of the points collected by the lidar and therefore allowing precise motion distortion correction. The drawbacks of these measurements are the computation time (due to the GP interpolations and the numerical integration) and the memory usage. As per the UPMs are relatively slow to compute, storing them is essential to limit the global execution time. On the other hand, UPMs need a significant amount of memory as each UPM is stored on at least 150 floating-point numbers (preintegrated measurements, covariance matrix, Jacobians for bias and time-shift corrections). Based on the Velodyne VLP-16 and double-precision floating-point numbers, it represents a memory consumption of more than 340MB per second of data solely to store the UPMs. To reduce the memory footprint and make IN2LAAMA executable on standard computers, only the UPMs associated to the last  $N_{UPM}$  frames are stored. As per the localisation and mapping procedure shown in Algorithm 2, choosing  $N_{UPM}$  equal to  $\max(N_g, N_e)$  does not impact the estimation time. However, this strategy requires the recomputation of all the UPMs to export the dense map when the estimation process terminates.

## VII. EXPERIMENTS AND RESULTS

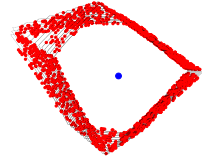
The proposed framework has been evaluated in simulation and on real data. Our real-world platform is a self-contained lidar and IMU sensor suite;

- Velodyne VLP-16, 16-channel ( $\pm 15^\circ$ ) lidar rotating at 10 Hz with a density of 300k point per second and noise of  $\pm 3$  cm.
- Xsens MTi-3, 3-axis accelerometer and 3-axis gyroscope sampling at 100Hz with noise of  $0.02 \text{ m/s}^2$  and  $0.097^\circ/\text{s}$ .

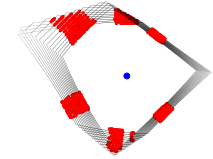
The simulated datasets have been generated to match the characteristics of the above mentioned system moving in a virtual room constituted of 7 planes. Both the back-end and front-end of the proposed method are tested and evaluated in our simulated experiments.



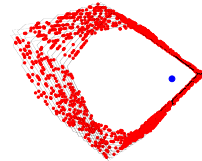
(a) Feature score histograms



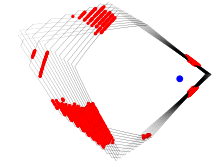
(b) IN2LAAMA



(c) [10]



(d) IN2LAAMA



(e) [10]

Fig. 7: Feature score comparison between IN2LAAMA and [10]. (a) represent the histograms of the score computed by each method. (b) and (c) show the scan used to generate (a) and display in red the 100 “most planar” points in each of the lidar channels according to the two methods. The blue dots represent the lidar position. (d) and (e) show another scan collected from a different position.

#### A. Simulation - Front-end

This subsection discusses the feature extraction of IN2LAAMA's front-end. Here we compare our approach with the front-end of [10]. We show that the feature extraction process of our method has a consistent behaviour with respect to the observed surface by using a scoring system invariant to the lidar viewpoint. In this regard, we have computed the feature score for each of the points of a simulated scan. The method presented in this paper computes a score that represents the cosine of the angle present in a patch. The higher the score is (with 1 being the maximum value), the more planar the patch is. In [10], the point score gives an evaluation of smoothness in a patch but does not correspond to any particular physical measurement of the actual geometry. Nonetheless, this score tends to be low in planar patches and higher in edge-like patches.

Fig. 7(a) shows the histograms of the scores in our simulated environment. We see in the left column that the scores computed by IN2LAAMA are consistent across the scan as per the bin around 1 dominates largely the histogram. The zoomed-in plot (second row) shows the modes associated to the different edges of the environment. However, with [10]'s scoring system

(inverse to ours) in the right column of Fig. 7(a), the distinction of the different types of surface is ambiguous.

The images (b) and (c) of Fig. 7 represent the scan used for the histograms generation. For each of the channels, the hundred points with the most planar score (higher score in ours and lower score in [10]) are shown in red. Fig. 7(d) and (e) show another scan collected in the same environment but from a different position. It is clear that IN2LAAMA's score computation provides a more consistent feature characterisation with respect to the actual geometry of the environment. Having features spread all across the scene leads to better stability during the estimation process.

### B. Simulation - Localisation and mapping

This set-up aims at evaluating different configurations of the proposed framework for localisation and mapping. The trajectories of the simulated sensor suite have been generated from sine functions with random frequencies and amplitudes. The extrinsic calibration between sensors is randomly generated for each trajectory. The results are evaluated over 10-run Monte Carlo simulations.

1) *Odometry*: First, we want to evaluate the advantages of using IMU factors for odometry-like localisation and mapping by comparing the accuracy of IN2LAAMA against our previous work [5]. To do so, we evaluate the localisation accuracy of IN2LAAMA with and without IMU factors on three sets of trajectories that have different level of angular velocities. The loop closure detection is deactivated for these experiments.

Table I displays the trajectories' parameters as well as the localisation errors against ground truth. In the case of low angular velocities (row "Slow"), both [5] and IN2LAAMA succeed in estimating the system pose. The integration of IMU factors improve slightly the trajectory estimate. Note that the presence of higher angular velocities leads to smaller overlap between lidar scans. Thus, the "Moderate" and "Fast" trajectories contain cases where the overlap between consecutive scans is not enough for the lidar factors to fully constrain the frame-to-frame motion. These "degenerated" trajectories trigger estimation failure of [5] but are correctly handled by the integration of frame-to-frame IMU factors.

2) *Loop-closure*: This set-up aims at demonstrating the ability of the proposed method to perform simultaneous localisation and mapping (SLAM) by integrating loop closures in the batch optimisation. A set of simulated trajectories is generated so that the first and last poses coincide. Table II shows the localisation results with and without the proposed loop closure detection method. The numbers show that loop closures help reducing both the frame-to-frame transformation error as well as the final pose error.

3) *Factor balance*: The afore-shown results are computed with realistic noise added to the simulated data as well as perfectly known extrinsic calibration. The following set-up has been designed to discuss the choice of the capping ratio  $\eta$  to balance the IMU and lidar factors in the estimation process. As mentioned in Section VI-B, in real data, the sensors do not always behave as per the manufacturer specifications or noise models, and the extrinsic calibration might not be accurately

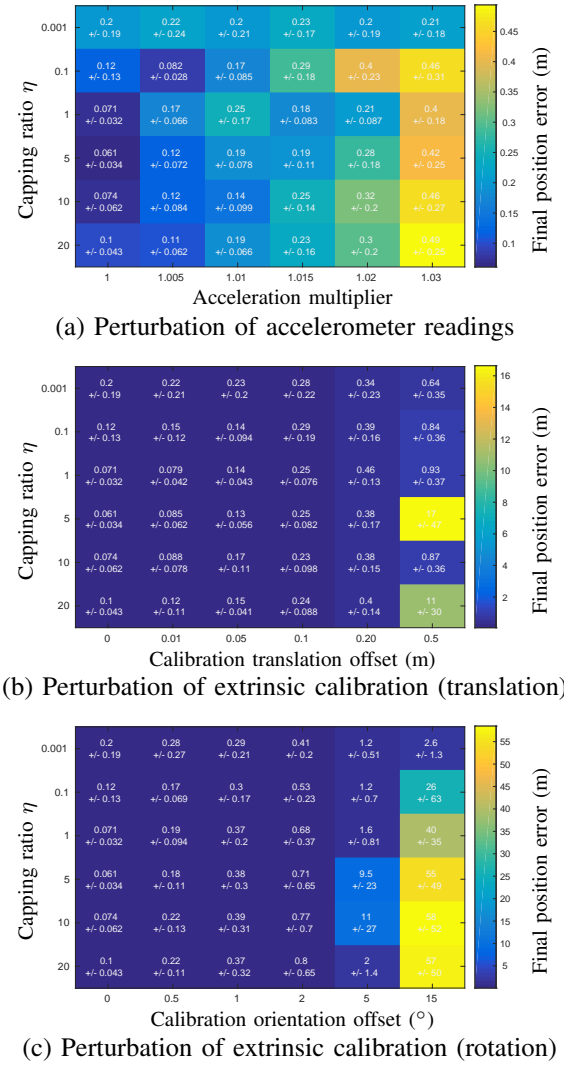


Fig. 8: Analysis of the capping ratio for different types and levels of perturbation in a 10-fold Monte Carlo simulation. The heatmaps represent the final position error in simulated environments. The set of trajectories used has an average length of 46.6 m, a mean velocity of 4.77 m/s and a mean angular velocity of 45.6 °/s.

known. These are the two scenarios that we are trying to emulate in this set-up.

To simulate the case of incorrectly modelled IMU data, we chose to perturb the IMU sensitivity by simply multiplying the accelerometer readings by a constant. Fig. 8(a) depicts the result obtained in the form of a heatmap. The plot shows that in the absence of perturbation, the system's accuracy benefits from "strong" IMU factors. On the other hand, when the inertial data is perturbed, a high  $\eta$  deteriorates significantly the results.

For the scenario when the extrinsic calibration is known inaccurately, we have distinguished two cases; inaccurate translation  $\mathbf{p}_T^L$  and inaccurate rotation  $\mathbf{R}_T^L$ . We have modelled these inaccuracies by adding constant offsets on each of the axes (in Euler angle representation for  $\mathbf{R}_T^L$ ). Fig. 8(b) and 8(c) show similar patterns as (a): to maximise the localisation

Motion type	Velocity (m/s)	Angular Vel. ( $^{\circ}/s$ )	Distance (m)	IMU factors	Num. fails	Final position error (m)	Final orientation error ( $^{\circ}$ )	Relative position error (m)	Relative orientation error ( $^{\circ}$ )
Slow	Avg 4.91	Avg 13.3	$292.2 \pm 22.7$	Yes	<b>0</b>	<b><math>0.21 \pm 0.14</math></b>	<b><math>0.52 \pm 0.27</math></b>	<b><math>0.001 \pm 1e-3</math></b>	<b><math>0.03 \pm 3e-3</math></b>
	Max 7.16	Max 19.9		No ([5])	<b>0</b>	$0.38 \pm 0.16$	$2.04 \pm 0.81$	$0.026 \pm 5e-3$	$0.06 \pm 1e-2$
Moderate	Avg 4.83	Avg 46.7	$286.9 \pm 11.5$	Yes	<b>0</b>	$0.35 \pm 0.33$	<b><math>0.76 \pm 0.43</math></b>	<b><math>0.003 \pm 1e-3</math></b>	<b><math>0.04 \pm 4e-3</math></b>
	Max 7.19	Max 75.1		No ([5])	2	<b><math>0.28 \pm 0.17</math></b>	$2.44 \pm 1.74$	$0.033 \pm 4e-3$	$0.07 \pm 8e-3$
Fast	Avg 4.95	Avg 117	$294.1 \pm 17.9$	Yes	<b>0</b>	<b><math>0.48 \pm 0.22</math></b>	<b><math>0.75 \pm 0.53</math></b>	<b><math>0.003 \pm 5e-4</math></b>	<b><math>0.05 \pm 6e-3</math></b>
	Max 7.81	Max 183		No ([5])	6	$0.54 \pm 0.26$	$2.47 \pm 0.55$	$0.045 \pm 6e-3$	$0.09 \pm 1e-2$

TABLE I: Quantitative results of the odometry set-up in simulated environment (10-run Monte Carlo simulation). The first four columns describe the dataset characteristics. The following columns show the errors on successful runs against the ground truth with (IN2LAAMA) and without ([5]) IMU factors.

Loop-closure	Final position error (m)	Final orientation error ( $^{\circ}$ )	Relative position error (m)	Relative orientation error ( $^{\circ}$ )
Without	$0.0979 \pm 0.0253$	$0.368 \pm 0.258$	$0.0010 \pm 0.0001$	$0.0260 \pm 0.0018$
	$0.0035 \pm 0.0018$	$0.024 \pm 0.012$	$0.0008 \pm 0.0001$	$0.0259 \pm 0.0019$
With				

TABLE II: Quantitative results of trajectory estimation when integrating loop closures constraints in the factor graph. The set of trajectories has the following characteristics: mean distance = 221 m, mean velocity = 3.72 m/s, mean angular velocity =  $8.53^{\circ}/s$ .

accuracy, the higher the perturbation is, the lower the capping ratio should be.

The intuition here is that in the presence of poorly modelled IMU data or inaccurate extrinsic calibration, it is better to “trust” the lidar than the IMU. This aligns with the exteroceptive nature of lidars against the proprioceptive nature of IMUs. On the other hand, IMU factors cannot be removed (by setting  $\eta = 0$ ) as some trajectories would not be observable. From these results, we propose a strategy to select the capping ratio in-between 1 and 5 for set-ups that provide accurate and reliable inertial data (high-quality IMUs), and when the extrinsic calibration is known, or at least, expected to be reasonable. In the presence of particularly poor IMU readings (low quality) or inaccurate calibration, the value of  $\eta$  can be chosen as low as 0.01-0.1.

### C. Simulation - Calibration

This set-up aims to evaluate quantitatively the accuracy of the proposed method when used for extrinsic calibration between a lidar and an IMU. These series of experiments were run on a set of trajectories of different durations. Table III shows the error of the calibration estimates. We can see that the accuracy of the estimate increase with the length of the dataset. These results demonstrate similar accuracy as our previous work [2] that relies on observing a calibration target made of at least three planes.

### D. Real-data - Localisation and mapping

Multiple datasets have been collected with our sensor suite inside the facilities of the University of Technology Sydney. These datasets have been made publicly available<sup>1</sup>. Moreover,

Trajectory duration (s)	Translation error (m)	Rotation error ( $^{\circ}$ )
9.8	$0.034 \pm 0.027$	$0.080 \pm 0.049$
39.2	$0.018 \pm 0.006$	$0.049 \pm 0.038$
59.5	$0.015 \pm 0.006$	$0.033 \pm 0.013$

TABLE III: Quantitative results for extrinsic calibration in simulated environment.

to demonstrate the versatility of the proposed method, we have applied IN2LAAMA to the MC2SLAM dataset [29]. This dataset has been selected because it contains timestamps for every single lidar point.

As mentioned above, our sensor suite comprises a *Velodyne VLP-16* and a low-cost *Xsens MTi-3* IMU. The *snark* driver<sup>2</sup> and the ROS Xsens driver<sup>3</sup> were used to collect the lidar and IMU data respectively. Lidar points and IMU measurements were logged with their associated timestamps. There is no explicit hardware or software mechanism for synchronisation between lidar and IMU data.

Note that in cluttered environments given sparse lidar data such as data from the VLP-16, the frame-to-frame data association of edge features will usually contain outliers that impact the state estimation. For the results presented in the rest of this paper, we have opted to use only planar features as the front-end of IN2LAAMA offers a more robust outlier rejection strategy for this type of features.

For quantitative comparisons, we chose to use metrics related to the planarity of planes in the environment as per none of the datasets used contains ground truth, neither for the trajectory nor the map. A video that shows 3D animations of the maps generated in this subsection is attached to this manuscript.

1) *Indoors*: This set-up aims to benchmark IN2LAAMA against our previous work [5] (no IMU factors) and the method in [10]. This last technique has been chosen for its top performance for lidar systems in the KITTI odometry benchmark [30]. Indoor datasets from two different locations have been used for this evaluation: in a lab environment and in a staircase between floors. In both cases, we will show that the proposed method outperforms both [5] and [10].

<sup>2</sup><https://github.com/acfr/snark>

<sup>3</sup>[http://wiki.ros.org/xsens\\_driver](http://wiki.ros.org/xsens_driver)

<sup>1</sup>[https://github.com/UTS-CAS/in2laama\\_datasets](https://github.com/UTS-CAS/in2laama_datasets)



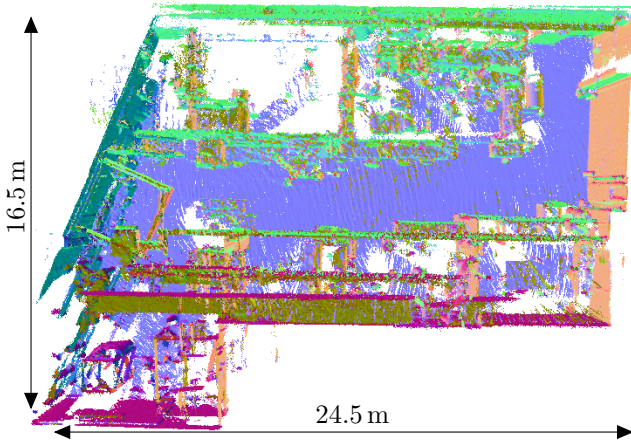


Fig. 9: Lab environment map generated with IN2LAAMA.

Dataset (plane used)	Average point-to-plane distance (mm)		
	[10]	[5]	IN2LAAMA
Lab (floor)	35	41	<b>26</b>
Staircase (wall)	70	37	<b>21</b>

TABLE IV: Quantitative comparison on real-data. The values shown corresponds to average point-to-plane distance between map points and the corresponding plane.

Fig. 9 shows the map<sup>4</sup> estimated by IN2LAAMA and Table IV, first row, shows quantitative comparison between the maps obtained from the different methods. The metric used is the average point-to-plane distance between the 3D-lidar points belonging to the ground and the ground plane. The ground plane is estimated by running a RANSAC-based plane fitting algorithm [31] on the manually segmented ground points. In this first dataset, [10] and [5] perform similarly while the proposed method leads to a slightly more accurate map.

The staircase dataset is more challenging because of the nature of the motion (dynamic with strong rotations) and the weak geometric information contained in some of the collected lidar scans. The maps generated with [10] and [5] are displayed in Fig. 10 and the one generated with the proposed method in Fig. 1. Irrespectively, whether it is only to help motion distortion correction as in [5] or to also fully constrain the pose-graph optimisation (IN2LAAMA approach), tightly integrating inertial information in the trajectory estimation leads to greater mapping accuracy than lidar-only techniques. The constant velocity motion assumption used in [10] reaches its limits in this kind of scenarios. To provide again a quantitative evaluation of the maps, point-to-plane distances are computed for points belonging to the same wall across the different floor levels (red rectangles in Fig. 10). The results are shown in the second row of Table IV.

Note that our framework uses extra information (IMU readings) in comparison to [10], and the incrementally built batch optimisation is not running real-time, thus the comparison is not totally fair. As an example, the staircase trajectory is

<sup>4</sup>The colours of the maps displayed in this section represent the post-computed normals of each point (computed using the 100 nearest points). Excluding some cropping to allow the reader to see inside the mapped structure, no other post-process have been performed.

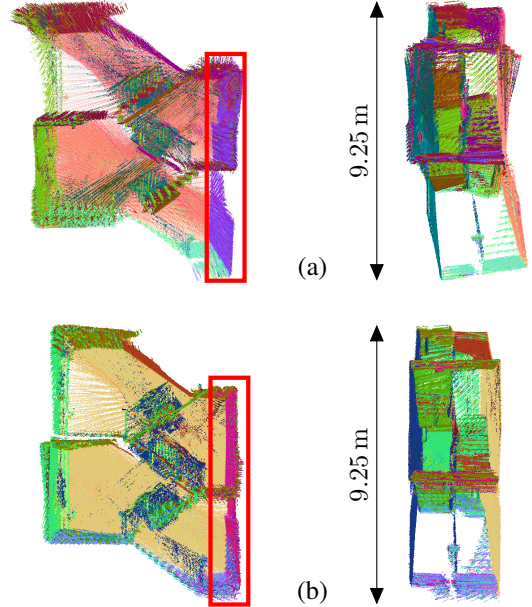


Fig. 10: Staircase maps generated with: [10] in (a), [5] in (b). The red rectangles highlight the wall used for the quantitative comparison. The map generated by IN2LAAMA is shown in Fig. 1.

estimated in 14 min on a standard Intel i5 CPU for a data recording of 35 s, that is 24 times slower than [10]. This run-time, however, can be hugely decreased by the use of an accurate prior and therefore reducing the number of batch optimisation performed. This is considered as part of our future work.

2) *Outdoors*: As mentioned above, the front-end of the proposed method has been designed for highly structured geometry. While the geometric features used are largely present in indoor environments, outdoor scenarios pose a challenge for our feature extraction algorithm.

We have chosen the MC2SLAM dataset [29] to show the performance of the proposed approach in an outdoor environment. The data has been acquired by a *Velodyne HDL-32* lidar and its built-in IMU mounted on top of a car that is driven around a University campus (sequence “campus\_drive” of [29]). Fig. 11 shows the map generated by IN2LAAMA with and without loop-closure. The trajectory is 409 m long and last 85.4 s. The drift accumulated before loop closure is 6.6° and 12.8 m.

At the start of the dataset, due to the translation-only trajectory, the accelerometer biases are not observable; the car is driven in a straight line for few meters (before starting a series of turns). Without any additional constraint on the accelerometer biases (Section VI-D) and given wrong initial orientation ( $\mathbf{R}_W^{T_0}$  arbitrarily flipped up-side down), the estimated state converges toward wrong biases values (magnitude of  $2g$ ). The extra factor on  $\hat{\mathbf{b}}_f^0$  provides the constraint required to contain the estimation error on the accelerometer biases while the lack of motion variation prevents the estimation to converge toward the true value of the state.

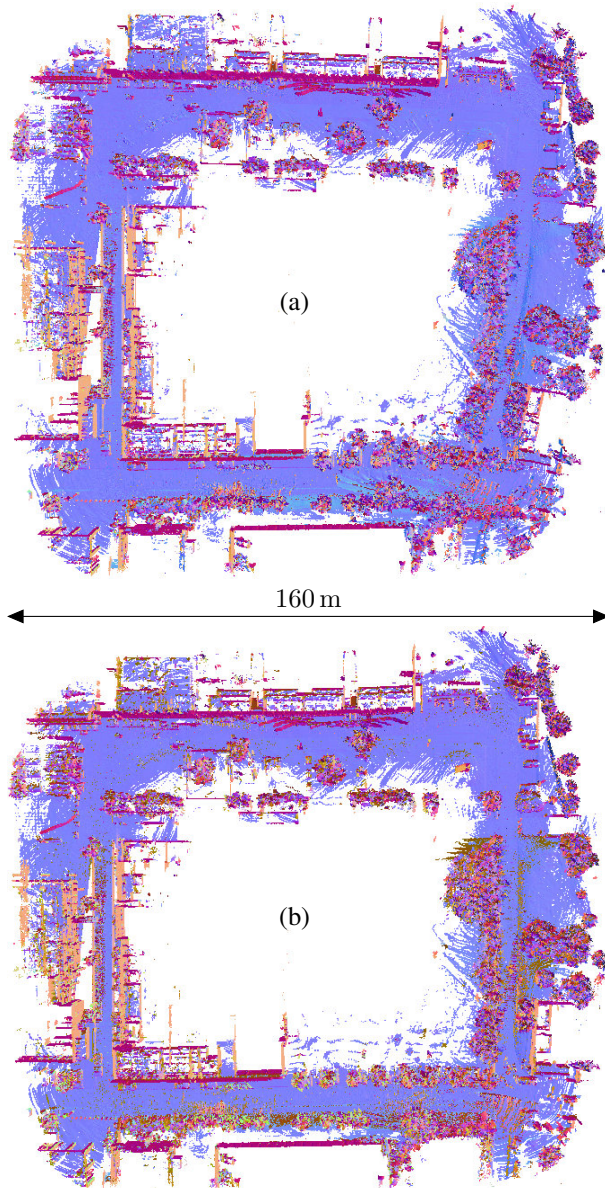


Fig. 11: Map generated by IN2LAAMA in outdoor environments (MC2SLAM dataset [29], sequence “campus\_drive”) without (a) and with (b) loop closure.

#### E. Real-data - Calibration

Finally, this set-up aims to evaluate the accuracy of the extrinsic calibration performed by the proposed framework. To do so, we have benchmarked our method against a “chained calibration” using an extra sensor, a global-shutter camera (Intel Realsense D435). The “chained calibration” computes IMU-camera and camera-lidar extrinsic calibrations and compound them together to obtain the IMU-lidar geometric transformation. The intrinsic camera calibration has been performed with *RADOCC* [32]. The IMU-camera geometric transformation has been estimated with *Kalibr* [20]. The camera-lidar extrinsic calibration is the result of the minimisation of point-to-plane distances of lidar points belonging to a checkerboard itself characterised by plane equations in the camera frame.

The evaluation is conducted by running the proposed method for localisation and mapping based on the calibration parameters obtained from the two calibration pipelines and using a capping ratio  $\eta$  equals to 1. The aggressive nature of the trajectory emphasises the need for good calibration to estimate an accurate map. In the resulting maps, average point-to-plane distances are computed between 3D points and the dominant plane in the scene. The chained calibration lead to a mean point-to-plane distance of 72 mm while IN2LAAMA’s map displayed more crispness with a mean point-to-plane distance of 40 mm.

The quality of the calibration results depend on the quality of the IMU readings as well as the environment and trajectory used for calibration. With IN2LAAMA’s front-end being built upon planar features the trajectory of the lidar need to allow the frame-to-frame registration of minimum 3 non-coplanar planes to properly constrain the lidar pose estimation. As demonstrated in [33], some trajectory types do not lead to observable calibration parameters. The ideal trajectories are random paths that stimulate the 6-DoF of the IMU.

## VIII. CONCLUSION

This paper introduced INertial Lidar Localisation Autocalibration And Mapping; a probabilistic framework for lidar-inertial localisation, mapping, and extrinsic calibration. The proposed method aims to deal with the motion distortion present in lidar scans without the need for an explicit motion model. The key idea is to use Upsampled Preintegrated Measurements to allow precise characterisation of the system’s motion during each lidar scan. The frame-to-frame scan registration is performed with a full batch on-manifold optimisation based on point-to-plane, point-to-line, and inertial residuals. The integration of IMU factors allows us to add robustness to highly dynamic motion. Extensive experiments have been conducted to demonstrate the performances of IN2LAAMA both on simulated and real-world data. A comparison with the state-of-the-art lidar localisation and mapping algorithm shows that our method performs better in indoor environments with challenging trajectories. However, while providing more accurate results, the current implementation of IN2LAAMA does not allow real-time operations.

Future work includes the exploration of different strategies and simplifications to make the method more efficient regarding computation time. We will also investigate the integration of a more robust and efficient loop closure detection mechanism. Alternative map representations such as using surfels will be investigated to integrate frame-to-model constraints in the optimisation and to improve the front-end robustness regarding weakly structured environments.

## REFERENCES

- [1] H. F. Durrant-Whyte, “An autonomous guided vehicle for cargo handling applications,” *International Journal of Robotics Research*, vol. 15, no. 5, pp. 407–440, 1996.
- [2] C. Le Gentil, T. Vidal-Calleja, and S. Huang, “3D Lidar-IMU Calibration based on Upsampled Preintegrated Measurements for Motion Distortion Correction,” *IEEE International Conference on Robotics and Automation*, 2018.



- [3] T. Lupton and S. Sukkariieh, "Visual-inertial-aided navigation for high-dynamic motion in built environments without initial conditions," *IEEE Transactions on Robotics*, vol. 28, no. 1, pp. 61–76, 2012.
- [4] C. Forster, L. Carlone, F. Dellaert, and D. Scaramuzza, "IMU preintegration on manifold for efficient visual-inertial maximum-a-posteriori estimation," *Robotics: Science and Systems*, pp. 6–15, 2015.
- [5] C. Le Gentil, T. Vidal-calleja, and S. Huang, "IN2LAMA : INertial Lidar Localisation And Mapping," *IEEE International Conference on Robotics and Automation*, 2019.
- [6] P. J. Besl and N. D. McKay, "A Method for Registration of 3-D Shapes," *IEEE Transactions on Pattern Analysis and Machine Intelligence*, 1992.
- [7] A. Segal, D. Haehnel, and S. Thrun, "Generalized-ICP," *Robotics: Science and Systems*, vol. 5, pp. 168–176, 2009.
- [8] E. Mendes, P. Koch, and S. Lacroix, "ICP-based pose-graph SLAM," *IEEE International Symposium on Safety, Security and Rescue Robotics*, pp. 195–200, 2016.
- [9] S. Hong, H. Ko, and J. Kim, "VICP: Velocity updating iterative closest point algorithm," *Proceedings - IEEE International Conference on Robotics and Automation*, no. Section 3, pp. 1893–1898, 2010.
- [10] J. Zhang and S. Singh, "LOAM : Lidar odometry and mapping in real-time," *Robotics: Science and Systems*, 2014.
- [11] M. Bosse and R. Zlot, "Continuous 3D Scan-Matching with a Spinning 2D Laser," *IEEE International Conference on Robotics and Automation*, 2009.
- [12] P. Furgale, T. D. Barfoot, and G. Sibley, "Continuous-Time Batch Estimation using Temporal Basis Functions," *IEEE International Conference on Robotics and Automation*, pp. 2088–2095, 2012.
- [13] S. Anderson and T. D. Barfoot, "Full STEAM ahead: Exactly sparse Gaussian process regression for batch continuous-time trajectory estimation on SE(3)," *IEEE International Conference on Intelligent Robots and Systems*, vol. 2015-Decem, no. 3, pp. 157–164, 2015.
- [14] D. Droschel and S. Behnke, "Efficient Continuous-time SLAM for 3D Lidar-based Online Mapping," *IEEE International Conference on Robotics and Automation (ICRA)*, no. May, pp. 5000–5007, 2018. [Online]. Available: [http://www.ais.uni-bonn.de/papers/ICRA\\_{\\_}2018\\_{\\_}Droschel.pdf](http://www.ais.uni-bonn.de/papers/ICRA_{_}2018_{_}Droschel.pdf)
- [15] M. Bosse, R. Zlot, and P. Flick, "Zebedee : Design of a spring-mounted 3-D range sensor with application to mobile mapping," *IEEE Transactions on Robotics*, vol. 28, no. October, pp. 1–15, 2012.
- [16] C. Park, P. Moghadam, S. Kim, A. Elfes, C. Foakes, and S. Sridharan, "Elastic LiDAR Fusion: Dense Map-Centric Continuous-Time SLAM," *IEEE International Conference on Robotics and Automation*, 2018. [Online]. Available: <http://arxiv.org/abs/1711.01691>
- [17] P. Geneva and K. Eickenhoff, "LIPS: LiDAR-Inertial 3D Plane SLAM [TR]," *IEEE International Conference on Intelligent Robots and Systems*, 2018.
- [18] J. Serafin, E. Olson, and G. Grisetti, "Fast and robust 3D feature extraction from sparse point clouds," *IEEE International Conference on Intelligent Robots and Systems*, vol. 2016-Novem, pp. 4105–4112, 2016.
- [19] J.-E. Deschaud, "IMLS-SLAM: scan-to-model matching based on 3D data," *IEEE International Conference on Robotics and Automation (ICRA)*, pp. 2480–2485, 2018. [Online]. Available: <http://arxiv.org/abs/1802.08633>
- [20] P. Furgale, J. Rehder, and R. Siegwart, "Unified temporal and spatial calibration for multi-sensor systems," *IEEE International Conference on Intelligent Robots and Systems*, pp. 1280–1286, 2013.
- [21] Z. Taylor and J. Nieto, "Parameterless automatic extrinsic calibration of vehicle mounted lidar-camera systems," *International Conference on Robotics and Automation: Long Term Autonomy Workshop*, no. October, pp. 3–6, 2014.
- [22] J. Castorena, U. S. Kamilov, and P. T. Boufounos, "Autocalibration of LIDAR and optical cameras via edge alignment," *IEEE International Conference on Acoustics, Speech and Signal Processing (ICASSP)*, pp. 2862–2866, 2016.
- [23] C. E. Rasmussen, C. K. I. Williams, G. Processes, M. I. T. Press, and M. I. Jordan, *Gaussian Processes for Machine Learning*, 2006.
- [24] J. L. Bentley, "Multidimensional binary search trees used for associative searching," *Communications of the ACM*, vol. 18, no. 9, pp. 509–517, sep 1975.
- [25] V. M. Tereshkov, "An Intuitive Approach to Inertial Sensor Bias Estimation," *International Journal of Navigation and Observation*, vol. 2013, pp. 1–6, 2013.
- [26] Z. Yu and J. L. Crassidis, "Accelerometer Bias Calibration Using Attitude and Angular Velocity Information," *Journal of Guidance, Control, and Dynamics*, vol. 39, no. 4, pp. 741–753, 2016.
- [27] S. Du, W. Sun, and Y. Gao, "Improving observability of an inertial system by rotary motions of an IMU," *Sensors (Switzerland)*, vol. 17, no. 4, pp. 1–20, 2017.
- [28] V. M. Tereshkov, "A Simple Observer for Gyro and Accelerometer Biases in Land Navigation Systems," *Journal of Navigation*, vol. 68, no. 04, pp. 635–645, 2015.
- [29] F. Neuhaus, T. Koß, R. Kohnen, and D. Paulus, "MC2SLAM: Real-Time Inertial Lidar Odometry Using Two-Scan Motion Compensation," *German Conference on Pattern Recognition*, 2018.
- [30] A. Geiger, P. Lenz, and R. Urtasun, "Are we ready for autonomous driving? the KITTI vision benchmark suite," *Proceedings of the IEEE Computer Society Conference on Computer Vision and Pattern Recognition*, pp. 3354–3361, 2012.
- [31] P. H. S. Torr and A. Zisserman, "MLESAC: A new robust estimator with application to estimating image geometry," *Computer Vision and Image Understanding*, vol. 78, no. 1, pp. 138–156, 1996.
- [32] A. Kassir and T. Peynot, "Reliable Automatic Camera-Laser Calibration," *Australasian Conference on Robotics and Automation*, 2010.
- [33] Y. Yang, P. Geneva, K. Eickenhoff, and G. Huang, "Degenerate Motion Analysis for Aided INS with Online Spatial and Temporal Sensor Calibration," *IEEE Robotics and Automation Letters*, vol. 4, no. 2, pp. 2070–2077, 2019.



**Cedric Le Gentil** received a DUT (two-year associate degree) in electrical engineering and industrial computing from the University Institute of Technology of Cachan (University of Paris XI) in 2012, and a master's degree in electronic and computer sciences from CentraleSupélec in 2015. He is currently working toward a PhD degree in robotics, started in 2017, at the Centre for Autonomous Systems at the University of Technology Sydney.



**Teresa Vidal-Calleja** received her BSc in Mechanical Engineering from the National Autonomous University of Mexico (UNAM), her MSc in Electrical Engineering (Mechatronics options) from CINVESTAV-IPN, Mexico City, and her PhD in Automatic Control, Computer Vision and Robotics from the Polytechnic University of Catalonia (UPC), Barcelona, Spain in 2007. She was a postdoctoral research fellow at both, LAAS-CNRS in Toulouse, France and the Australian Centre for Field Robotics at the University of Sydney, Australia. She joined the

Centre for Autonomous Systems at University of Technology Sydney (UTS) in 2012, where was UTS Chancellors Research Fellow and later became Senior Lecturer. She has been visiting scholar at the Active Vision Laboratory of the University of Oxford, UK and, more recently, at the Autonomous Systems Lab, ETHZ, Switzerland. Her research interests are in robotic perception and estimation; including automatic recognition, multimodal sensor fusion, mapping, SLAM, aerial and ground cooperative robots cooperation, and autonomous navigation.



**Shoudong Huang** received the Bachelor and Master degrees in Mathematics, Ph.D in Automatic Control from Northeastern University, P.R. China in 1987, 1990, and 1998, respectively. After his PhD study, he worked at the University of Hong Kong for 1.5 years and The Australian National University for 2 years as a Research Fellow in control area. He joined the Australian Research Council (ARC) Centre of Excellence for Autonomous Systems in 2004 and started to work in robotics area. He is currently an Associate Professor at Centre for Autonomous

Systems, Faculty of Engineering and Information Technology, University of Technology, Sydney, Australia. His research interests include mobile robots simultaneous localization and mapping (SLAM), exploration and navigation and nonlinear system control. He has published more than 150 papers in robotics and control area. He is currently serving as an Associate Editor for IEEE Transactions on Robotics.